Tribology International 140 (2019) 105873

Contents lists available at ScienceDirect

Tribology International

journal homepage: www.elsevier.com/locate/triboint

An extended Elrod-Adams model to account for backpressure and blow-by inception

Alfredo Jaramillo*, Gustavo C. Buscaglia

Instituto de Ciências Matemáticas e de Computação, Universidade de São Paulo, 13560-970, São Carlos, Brazil

ARTICLE INFO

Keywords:
Piston-ring-liner
Combustion chamber pressure
Elrod-adams model
Blow-by

ABSTRACT

The Piston-Ring-Liner system is the main tribological component of internal combustion engines. Hydrodynamic models are customarily used to numerically assess the performance of different ring designs and liner surface treatments. However, available models do not properly incorporate the backpressure boundary condition, which corresponds to the combustion chamber pressure and is quite significant. A new model is proposed here that imposes the combustion-chamber pressure in a mass-conserving and physically realistic way, together with an effective algorithm for its numerical approximation. The new model incorporates the pressure difference across the ring, which is shown to have a substantial effect on the predicted friction force and film thickness. The model is further elaborated so as to provide a criterion for predicting blow-by inception.

1. Introduction

Hydrodynamical models are used to estimate load carrying capacity, friction losses and minimum film thickness (MFT) of several tribological devices that involve cavitation, which is a non-linear rupture of the fluid continuity [1]. In this work we focus on the Piston-Ring-Liner (PRL) mechanism, which exhibits some unique features that make its modeling especially challenging. The PRL consists of a piston moving inside a cylinder, as schematized in Fig. 1. One or more sealing rings slide against the cylinder liner, which to reduce friction is covered by a thin layer of oil. On both sides of the ring the oil does not completely fill the gap between piston and liner, so that suitable models need to consider *partial-film* conditions there [2]. What complicates things is that the partial films on both sides of the ring are not at the same pressure. While the crankcase side is essentially at constant pressure, the other side is exposed to the combustion chamber pressure (CCP) which changes with time and reaches values of up to 100 atm.

The effect of the CCP on the PRL mechanism is twofold: On one hand, it has a sealing effect by exerting an additional force on the back of the ring that pushes it against the liner. On the other hand, the CCP modifies the pressure (and thus the oil flow) in the full-film region that develops between the ring and the liner, since mechanical equilibrium ensures that the pressure on the combustion-chamber-side boundary of that region must equal the CCP. This latter effect increases both the lift force on the ring and the oil flow rate towards the crankcase side of the ring. In some severe cases the oil flow generated by the pressure difference across the ring can be so high as to create a gas channel through which the CCP would leak towards the crankcase. Such phenomenon, which is both mechanically and environmentally quite negative, will be denoted here as *blow-by* Ref. [3].

Few simulations of the PRL mechanism under the conditions of a functioning internal combustion engine can be found in the literature. Han & Lee [2] simplified the geometry to one-dimensional by assuming uniformity along the circumferential direction and solved it with the correct boundary condition on the combustion-chamber side. They thus considered both effects of the CCP and showed that their impact on the numerical predictions is significant. Their approach, as that of Mufti et al. [4], is restricted to one-dimensional geometries. Other studies have opted to only consider the sealing effect of the CCP, disregarding its effect on the hydrodynamical pressure field. Such is the case of Checo et al. [5–7] and of Hu et al. [8], which impose zero boundary conditions on the hydrodynamic pressure.

In the works of Kligerman & Shinkarenko [9], Usman & Park [10] and Chong et al. [11,12] the boundary conditions on the hydrodynamic pressure were set to CCP on the combustion-chamber side. Full engine cycles simulations were performed and tribological quantities like MFT and friction loss were computed taking into account the CCP dependence on time. The cavitation models adopted in these works, however, involve complementarity conditions between pressure and fluid-film content. As a result, a full-film is automatically assumed at any boundary where the pressure is above saturation, in particular at the combustion-chamber end of the simulation domain where in fact the

* Corresponding author.
E-mail address: ajaramillopalma@gmail.com (A. Jaramillo).

https://doi.org/10.1016/j.triboint.2019.105873
Received 6 May 2019; Received in revised form 29 June 2019; Accepted 14 July 2019
Available online 17 July 2019

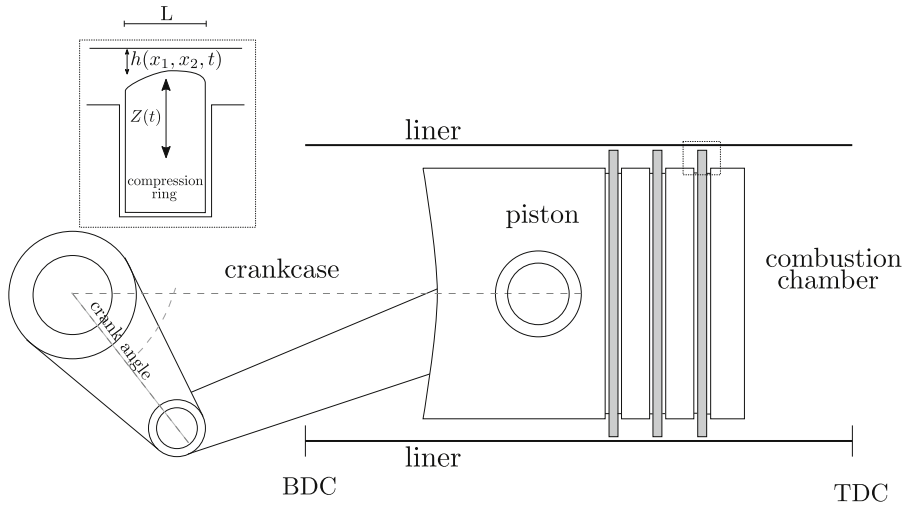

Fig. 1. Scheme of the Piston-Ring-Liner system.

flow is separated. This creates unphysical full-film regions which may have a strong impact on the pressure build-up and thus on the tribological assessments.

In this work we propose a modification of the Elrod-Adams cavitation model adopted by Chong et al. [11,12] so that non-homogeneous pressure conditions on the combustion-chamber-side boundary can be imposed without creating unphysical full-film regions. Remarkably, this requires some major overhauling of both the mathematical model (see Section 2) and the numerical algorithm used to solve it (see Section 3), since a new (and strong) nonlinearity is added. The new model, which preserves the mass-conservation property of the Elrod-Adams model, is assessed numerically in Section 4. We start from simple cases to develop some intuition on its behavior, which in all cases is physically realistic. Special care is taken to show that the numerical solutions remain stable and converge under both spatial and temporal refinement of the discretization. We finally discuss simulations of the full engine cycle considering time-dependent CCP and in one- and two-dimensional geometries. They illustrate the various complex phenomena that can be captured with the proposed model. In particular, we show that the model is capable of modeling blow-by inception and propose, for the first time, an objective criterion for its prediction.

2. Mathematical models

The main components of the PRL system are depicted in Fig. 1, here a simplified modeling of that system is assumed as described below. The fundamental scales are given in Table 1 and the nomenclature for the non-dimensional quantities is given in Table 2.

2.1. Geometrical model and ring dynamics

The liner is assumed to be perfectly smooth and cylindrical, so that the gap between the surfaces is modeled by the function

$$h(x_1, x_2, t) = Z(t) + h^{R}_{\text{ring}}(x_1, x_2) + h^{\delta}_{\text{wear}}(x_2), \tag{1}$$

Table 1
Fundamental scales.

Symbol	Value	Units	Description
H	1×10^{-6}	m	Gap thickness
L	1×10^{-3}	m	Scale on the x_1-x_2 plane
μ	4×10^{-3}	Pa·s	Lubricant viscosity
U	10	m/s	Reference speed along the x_1 axis

Table 2
Nomenclature: non-dimensional quantities and their corresponding scale.

Quantity	Description	Scale
x_1	Longitudinal coordinate	L
x_2	Transverse coordinate	L
t	Time	L/U
h, h_{ring}, h^{δ}_{wear}	Functions defining the surfaces gap	H
h_{feed}	Film thickness at the boundaries	H
u	Liner's speed along x_1	U
Z	Minimum gap in time	H
L_{ring}	Ring's length along x_1	L
B	Bore radius	L
p	Hydrodynamic pressure	$6\mu\, UL/H^2$
W^{h}, W^{ps}, W^{c}	Radial forces per unit width	$6\mu\, UL^2/H^2$
m	Ring's mass per unit width	$6\mu L^4/(H^3U)$
μ_{c}	Boundary friction coefficient (= 0.11)	-

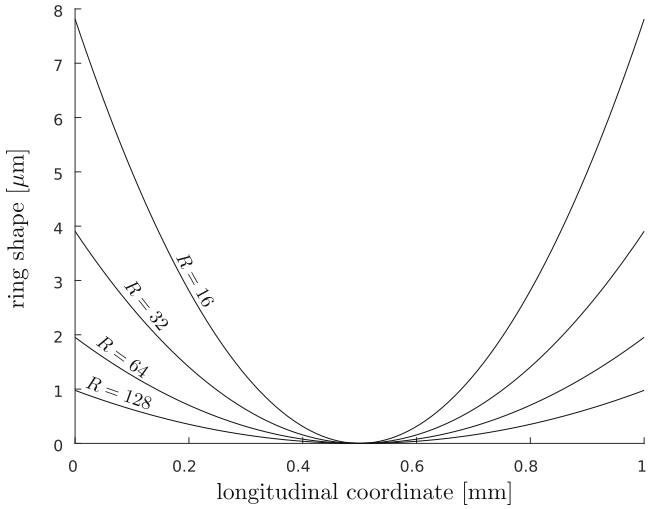

Fig. 2. Basic ring shape function h^{R}_{ring} along the x_1-axis for different values of R.

where Z is the dynamic variable accounting for the expansion/contraction of the ring, h^{R}_{ring} is the function describing the ring's shape, defined as satisfying $\min_{\mathbf{x}} h^{R}_{\text{ring}}(\mathbf{x}) = 0$, and for which we adopt the basic parabola depicted in Fig. 2 and written as

$$h^{R}_{\text{ring}}(x_1, x_2) = \frac{L}{H}\frac{(x_1 - 0.5)^2}{2R}, \tag{2}$$

where R is the curvature radius of the ring profile. Later on a case in which a texture is added to h^{R}_{ring} is also considered. For later use we have also introduced h^{δ}_{wear}, which is a function modeling a non-homogeneous wear of the surfaces along the circumferential direction. For simplicity, this function is assumed to have a Gaussian profile centered at the circumferential angle equal to π:

$$h^{\delta}_{\text{wear}}(x_2) = \delta \exp(-(x_2 - \pi B)^2/c^2) \qquad x_2 \in [0,2\pi B]. \tag{3}$$

The ring follows a reciprocal motion along the x_1-axis and its speed is denoted by $u(t)$. The dynamics of $Z(t)$ is determined by Newton's equation:

$$m\frac{d^2Z}{dt^2} = W^{\text{h}}(t) + W^{\text{ps}} + W^{\text{con}}(h) + W^{\text{cc}}(t). \tag{4}$$

The first term on the right-hand side corresponds to the hydrodynamical force (per unit width in the circumferential direction), computed as

$$W^{\text{h}}(t) = \frac{1}{B}\int_0^{2\pi B}\int_0^1 p(x_1, x_2, t)\, dx_1\, dx_2, \tag{5}$$

the second and third terms correspond to the applied pre-stress load (datum) and the contact load, respectively, the latter being computed by means of the Greenwood-Tripp model [13] as

$$W^{\text{con}}(h) = \frac{1}{B}\int_0^{2\pi B}\int_0^1 p^{\text{con}}(h(x_1, x_2, t))\, dx_1\, dx_2, \tag{6}$$

with the contact pressure p^{con} given by

$$p^{\text{con}}(h) = \pi\frac{16\sqrt{2}}{15}(\eta\beta\sigma)^2\sqrt{\sigma/\beta}E'F_{5/2}(h/\sigma) = K'E'F_{5/2}(h/\sigma), \tag{7}$$

where E' is the composite modulus of elasticity, and η, β and σ are the asperity density, radius of curvature and composite standard deviation of the asperities' height. In this work we adopt $E' = 100$ GPa, $\sigma = 0.48$ μm and the correlation parameter $K' = 0.02$, which are typical values for the PRL system [14]. The value of $F_{5/2}(h/\sigma)$ corresponds to an integral that is approximated as done by Panayi-Schock in Ref. [15]. The last term in Eq. (4) corresponds to the pressure exerted on the back of the ring, pushing it towards the liner and modeled by

$$W^{\text{cc}}(t) = -\gamma\, p_{\text{cc}}(t)\, L_{\text{ring}} \tag{8}$$

where γ is the back-pressure factor and L_{ring} is the ring's length along the x_1 direction.

The friction force exerted by the fluid on the ring at time t along the x_1-axis is given by Ref. [16].

$$F(t) = -\frac{1}{B}\int_0^{2\pi B}\int_a^b\left(-\frac{\mu u}{h}g(\theta) + \frac{h}{2}\frac{\partial p}{\partial x_1} + p\frac{\partial h_{\text{ring}}}{\partial x_1} - \mu_{\text{c}}\, p^{\text{con}}\right)dx_1\, dx_2, \tag{9}$$

where

$$g(\theta) = \begin{cases}\theta & \text{if } \theta > \theta_{\text{s}}\\ 0 & \text{otherwise}\end{cases}, \tag{10}$$

and μ_{c} is the boundary friction coefficient. The threshold θ_{s} is interpreted as the minimum oil fraction for shear forces to be transmitted between the surfaces and it was set to 0.95 (e.g. Ref. [5]).

2.2. Hydrodynamics and cavitation modeling

The hydrodynamical pressure p and the saturation field θ are modeled by an extension of the Elrod-Adams cavitation model that reads

$$\nabla\cdot\left(\frac{h^3}{2}\nabla p\right) = \frac{u(t)}{2}\frac{\partial h\theta}{\partial x_1} + \frac{\partial h\theta}{\partial t}, \tag{11}$$

along with the restrictions for the unknown fields

$$p \geq T(\theta) \qquad \text{and} \qquad 0 \leq \theta \leq 1, \tag{12}$$

the boundary conditions

$$\begin{cases} p(0, x_2, t) = 0, & p(1, x_2, t) = p_{\text{cc}}(t)\\ \theta(0, x_2, t) = \frac{h_{\text{feed}}}{h(0, x_2, t)}, & \theta(1, x_2, t) = \frac{h_{\text{feed}}}{h(1, x_2, t)}\end{cases} \qquad \text{for } x_2 \in \left[0,2\pi B\right], \tag{13}$$

periodic conditions along the x_2-axis and the complementarity conditions

$$(p - T(\theta))(1 - \theta) = 0. \tag{14}$$

The novelty of this model lies in the operator T. When $T(\theta) \equiv 0$ one recovers the classical Elrod-Adams model, which essentially assumes a zero combustion-chamber pressure. Let us denote by $\Omega_0 = \{\mathbf{x} \in \Omega\colon \theta(\mathbf{x}) < 1\}$ the region of the domain where the film is not complete, which in general has many connected components. The basic idea of the model proposed here is that the connected component of Ω_0 that touches the right boundary must have T equal to the combustion-chamber pressure, while in the others $T \equiv 0$. More specifically, denoting by Ω_0^{r} the connected component of Ω_0 that intersects the set $\{(x_1, x_2) \in \Omega\colon x_1 = 1\}$, we define

$$T(\theta)(\mathbf{x}) = \begin{cases} p_{\text{cc}}(t) & \text{for } \mathbf{x} \in \Omega_0^{\text{r}}\\ 0 & \text{otherwise}\end{cases}. \tag{15}$$

An example of this is shown in Fig. 3. Notice that if the right and left sides of the system are connected by a "channel" of incomplete film, i.e., if the intersection $\Omega_0 \cap \Omega_0^{\text{r}}$ is non-empty and $p_{\text{cc}}(t) > 0$, the model becomes undefined. This condition intuitively determines the blow-by of combustion chamber gases, and will be further discussed later on.

As in the case of the standard Elrod-Adams model, the extended model consists of a transport equation on Ω_0 and an elliptic equation on the full-film region. Though the standard model enforces mass

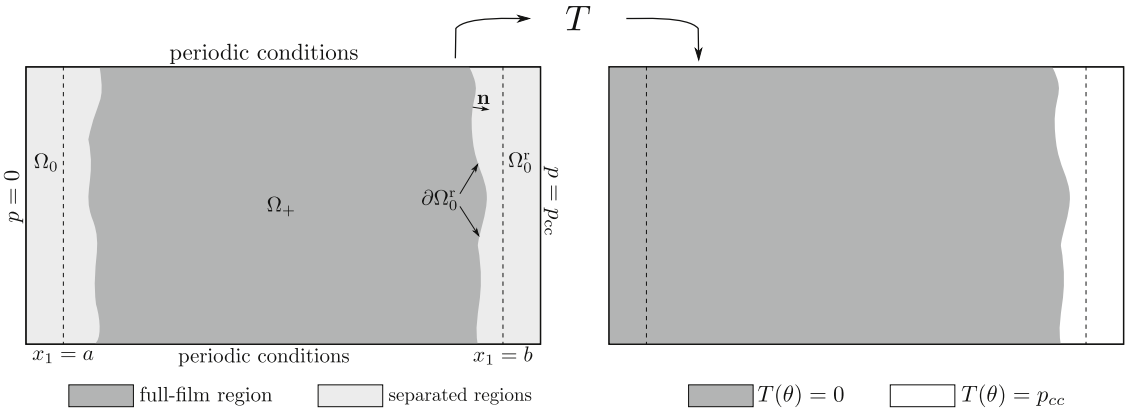

Fig. 3. Scheme of the operator T.

conservation throughout the domain, when $p_{cc} > 0$ a supplementary boundary condition must be supplied at rupture points. In fact, on the boundary of the full-film region ($\partial\Omega_+$) the mass conservation condition can be written, assuming h to be continuous, as

$$\frac{\partial p}{\partial \mathbf{n}} = 2\frac{(1-\theta_-)}{h^2}\left(\frac{U}{2}\mathbf{e}_c - \mathbf{V}^i\right)\cdot\mathbf{n}, \tag{16}$$

where θ_- is the value of θ at the cavitated/separated side, $\mathbf{e}_c$ is the unit vector along the Couette flux, $\mathbf{V}^i$ is the interface velocity and $\mathbf{n}$ is the outward normal to $\partial\Omega_+$. This last condition implies

$$\begin{cases} \frac{\partial p}{\partial \mathbf{n}} \geq 0 & \text{at rupture points} \\ \frac{\partial p}{\partial \mathbf{n}} \leq 0 & \text{at reformation points} \end{cases},$$

which when $T \equiv 0$ corresponds to the null-gradient condition at the rupture points but, when $p_{cc} > 0$, is not enough to assure the well-posedness of the extended model [17–19]. To tackle this issue, in this work the condition $\frac{\partial p}{\partial \mathbf{n}} = 0$ is imposed at the rupture points. This can be summarized as

$$\frac{\partial p}{\partial \mathbf{n}} \leq 0 \qquad \text{in } \partial\Omega_+. \tag{17}$$

This condition, as detailed in the next section, is numerically implemented by extending $T(\theta)$ one cell into Ω_+.

3. Numerical method

The domain Ω is divided in $N_{x_1} \times N_{x_2}$ cells and a finite volume scheme for Eq. (11) is used. For this, the x_1 flux component going from node $(i-1, j)$ to node (i, j) is discretized by

$$-\frac{h^3}{2}\frac{\partial p}{\partial x_1} + \frac{u}{2}h\theta \simeq -\frac{1}{2}\frac{(h^n_{i-1,j})^3 + (h^n_{i,j})^3}{2}\frac{p^n_{i,j} - p^n_{i-1,j}}{\Delta x_1} + \frac{u}{2}h^n_{i-1,j}\theta^n_{i-1,j}, \tag{18}$$

where an upwind approximation is used for the Couette term. Balancing the fluxes on each cell and discretizing time along an implicit scheme for the temporal term $\frac{\partial h\theta}{\partial t}$ one gets the system of equations:

$$a^{00}_{i,j}\, p^n_{i,j} + e^{00}_{i,j}\,\theta^n_{i,j} = C_{i,j}(\boldsymbol{p}^n, \theta^n), \tag{19}$$

$$p^n_{i,j} \geq T(\theta^n)_{i,j}, \tag{20}$$

$$0 \leq \theta^n_{i,j} \leq 1, \tag{21}$$

$$\left(p^n_{i,j} - T(\theta^n)_{i,j}\right)(1-\theta^n_{i,j}) = 0, \tag{22}$$

where

$$C_{i,j}(\boldsymbol{p}^n, \theta^n) = -a^{-0}_{i,j}p^n_{i-1,j} - a^{+0}_{i,j}p^n_{i+1,j} - a^{0+}_{i,j}p^n_{i,j+1} - a^{0-}_{i,j}p^n_{i,j-1} - e^{-0}_{i,j}\theta^n_{i-1,j} + f^n_{i,j}, \tag{23}$$

with

$$a^{00}_{i,j} = s^n_{i+1,j} + s^n_{i-1,j} + (\Delta x_1/\Delta x_2)^2 (s^n_{i,j+1} + s^n_{i,j-1}) \qquad e^{00}_{i,j} = (u\,\Delta x_1 + 2\Delta x_1^2/\Delta t)h^n_{i,j},$$
$$a^{+0}_{i,j} = -s^n_{i+1,j}, \qquad a^{-0}_{i,j} = -s^n_{i-1,j},$$
$$a^{0-}_{i,j} = -(\Delta x_1/\Delta x_2)^2\, s^n_{i,j-1}, \qquad a^{0+}_{i,j} = -(\Delta x_1/\Delta x_2)^2\, s^n_{i,j+1},$$
$$e^{-0}_{i,j} = -u\,\Delta x_1\, h^n_{i-1,j}, \qquad s^n_{i\pm1,j\pm1} = \tfrac{1}{2}((h^n_{i,j})^3 + (h^n_{i\pm1,j\pm1})^3),$$
$$f^n_{i,j} = 2\Delta x_1^2/\Delta t\; h^{n-1}_{i,j}\theta^{n-1}_{i,j}.$$

Notice that $a^{00}_{i,j}$, $e^{00}_{i,j}$, $f^n_{i,j}$ are non-negative, and each term $a^{+0}_{i,j}$, $a^{-0}_{i,j}$, $a^{0+}_{i,j}$, $a^{0-}_{i,j}$, $e^{-0}_{i,j}$ is non-positive, thus $C_{i,j}(\boldsymbol{p}^n, \theta^n) \geq 0$.

The computation of the discrete field $T(\theta^n)_{i,j}$ is performed as follows (see Fig. 4): A flooding algorithm identifies all cells with $\theta^n_{i,j} < 1$ that are connected to the combustion-chamber side of the domain boundary (orange cells in the figure). This set of cells is then enlarged with those cells that are adjacent to the previous ones either vertically or horizontally (green cells in the figure). The resulting set of cells is denoted by I_r, and then the discrete operator T results from

$$T(\theta^n)_{i,j} = \begin{cases} p_{cc}(t) & \text{if } (i,j) \in I_r\,, \\ 0 & \text{otherwise.} \end{cases} \tag{24}$$

It is noteworthy that the system of equations 19–22 can be written as a fixed-point problem. For this purpose, consider an operator that maps a pair $(\boldsymbol{p}, \theta$ of discrete pressure and saturation fields into another similar pair defined as follows:

$$B_T(\boldsymbol{p}, \theta)_{i,j} = \begin{cases} \left(\frac{C_{i,j}(\boldsymbol{p},\theta) - e^{00}_{i,j}}{a^{00}_{i,j}\,T(\theta)_{i,j}},\ 1\right) & \text{if } \frac{C_{i,j}(\boldsymbol{p},\theta) - e^{00}_{i,j}}{a^{00}_{i,j}\,T(\theta)_{i,j}} \geq 0 \\ \left(T(\theta)_{i,j},\ \frac{C_{i,j}(\boldsymbol{p},\theta) - a^{00}_{i,j}\,T(\theta)_{i,j}}{e^{00}_{i,j}}\right) & \text{if } \frac{C_{i,j}(\boldsymbol{p},\theta) - e^{00}_{i,j}}{a^{00}_{i,j}\,T(\theta)_{i,j}} < 0 \end{cases}, \tag{25}$$

With this definition, the system (19)–(22) can be rewritten as the fixed point problem

$$B_T(\boldsymbol{p}^n, \theta^n) = (\boldsymbol{p}^n, \theta^n). \tag{26}$$

The proposed algorithm (Algorithm 1) exploits this fixed-point structure, following ideas proposed by Alt [20], Marini & Pietra [21] and Ausas et al. [22]. Notice that the dynamics of the ring is treated with a Newmark scheme.

Remark: Though by construction the solution of (26) satisfies (19), (20), (22) and $\theta^n_{i,j} \leq 1$, the satisfaction of $\theta^n_{i,j} \geq 0$ depends on the precise definition of the operator T. In fact, if the green cells in Fig. 4 are not added to the set I_r in which $T(\theta) = p_{cc}$, then the non-negativity of $\theta^n_{i,j}$ cannot be guaranteed. Going back to a physical interpretation, the proposed definition of I_r imposes the value zero to the normal derivative of the pressure at rupture boundaries.

Algorithm 1. Adaptation of the numerical algorithm presented by Ref. [20] to solve system (26).

Input: h: gap function; $\boldsymbol{p}^{n-1}$, $\boldsymbol{\theta}^{n-1}$, Z^{n-1}, V^{n-1}: initial guess
begin
  $k = 1$;
  $\boldsymbol{p}^{n,0} = \boldsymbol{p}^{n-1}$; $\boldsymbol{\theta}^{n,0} = \boldsymbol{\theta}^{n-1}$; $Z^{n,0} = Z^{n-1}$;
  $\boldsymbol{p}^{n,k} = \boldsymbol{p}^{n,0}$; $\boldsymbol{\theta}^{n,k} = \boldsymbol{\theta}^{n,0}$; $Z^{n,1} = Z^{n-1}$;
  while *change* $>$ *tol* **do**
    $W^{h;n,k} = (1/B)\,\Delta x_1\,\Delta x_2 \sum_{i,h} p^{n,k-1}_{i,j}$;
    $W^{c;n,k} = (1/B)\,\Delta x_1\,\Delta x_2 \sum_{i,h} p^{n,k-1}_{c;i,j}$;
    $Z^{n,k} = Z^n + \Delta t\, V^{n-1} + \Delta t^2/(2\,m)(W^{h;n,k} + W^{c;n,k} + W^a(t^n))$;
    compute $T(\boldsymbol{\theta}^{n,k-1})$;
    for $i = 1 \ldots N_{x_1}$, $j = 1 \ldots N_{x_2}$ **do**
      if $(C_{i,j} - e^{00}_{i,j})/a^{00}_{i,j} \geq T(\boldsymbol{\theta}^{n,k-1})_{i,j}$ **then**
        $p^{n,k}_{i,j} = (C_{i,j} - e^{00}_{i,j})/a^{00}_{i,j}$;
        $\theta^{n,k}_{i,j} = 1$;
        else
          $\theta^{n,k}_{i,j} = (C_{i,j} - a^{00}_{i,j}\,T(\boldsymbol{\theta}^{n,k-1})_{i,j})/e^{00}_{i,j}$;
          $p^{n,k}_{i,j} = T(\boldsymbol{\theta}^{n,k-1})_{i,j}$;
        end
      end
    end
    change $= \|\boldsymbol{p}^{n,k} - \boldsymbol{p}^{n,k-1}\| + \|\boldsymbol{\theta}^{n,k} - \boldsymbol{\theta}^{n,k-1}\| + \|Z^{n,k} - Z^{n,k-1}\|$;
    $\boldsymbol{p}^{n,k+1} = \boldsymbol{p}^{n,k}$; $\boldsymbol{\theta}^{n,k+1} = \boldsymbol{\theta}^{n,k}$; $Z^{n,k+1} = Z^{n,k}$;
    $k = k + 1$;
  end
  $V^n = V^{n-1} + (\Delta t/m)(W^{h;n,k} + W^{c;n,k} + W^a(t^n))$;
  return $\boldsymbol{p}^{n,k}$, $\boldsymbol{\theta}^{n,k}$, $Z^{n,k}$, V^n;
end

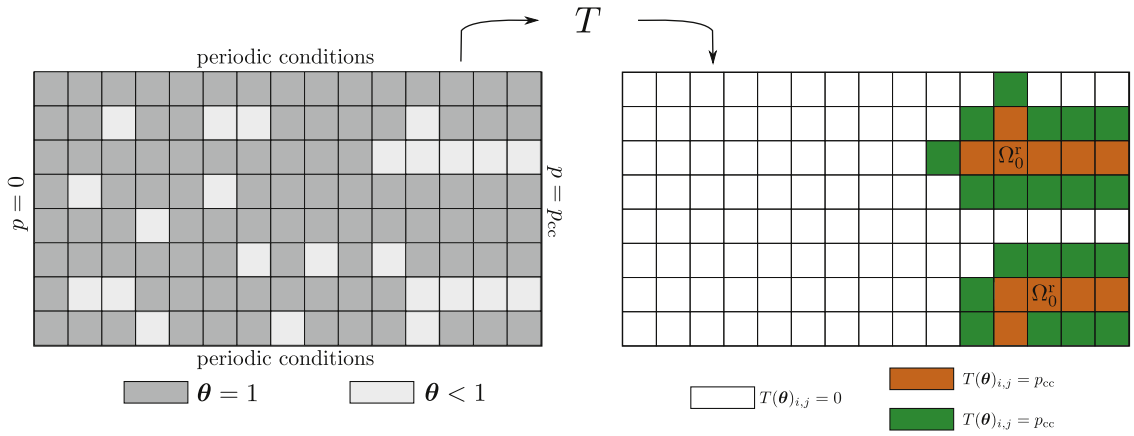

Fig. 4. Illustration of the action of the discrete operator T on a discrete saturation field θ.

4. Numerical examples

The nonlinearity of the proposed model is quite strong. At each time, the rightmost connected component of the cavitated/separated region must be identified to compute the operator T. Further, as a way to impose the zero normal pressure gradient at rupture points, T is extended by one cell outside the numerical boundary of this connected component. Though the model is consistent with the physics, it may well be ill-posed, which would result in a chaotic behavior of the numerical solution as the mesh and the time step are refined. Convergence analyses in non-trivial cases are thus crucial to assess the model and its numerical implementation. Such analyses, with increasing complexity, are reported in what follows.

For the following simulations the bore radius is set to $B = 41$, the ring's length along x_1 to $L_{\text{ring}} = 1$, the ring mass to $m = 1.25 \times 10^{-5}$ and the pre-stress load to $W^{\text{ps}} = -1.666 \times 10^{-4}$ (the corresponding dimensional values are 4.1 cm, 1 mm, 0.03 kg/m and − 40 N/m, respectively). The back-pressure factor is set to $\gamma = 0.9$.

4.1. One-dimensional stationary solutions

We begin by illustrating the model's behavior through a series of stationary solutions assuming different values for p_{cc} (constant in time). The ring-to-liner distance Z is also fixed to unity. The solutions are obtained by means of transient simulations for a time length t_f big enough such that no variation on $\boldsymbol{p}$ or θ is observed for $t > t_f$. Based in a convergence analysis exposed in the next section, the cell size and time step length are chosen as $\Delta x_1 = 0.005$ and $\Delta t = 0.01$.

The pressure and saturation fields obtained for different values of p_{cc} are shown in Fig. 5 when the lower surface is moving to the right ($u = 1$). The pressure equals p_{cc} for all $x_1 \geq \beta$ as expected, the point β being in this case a rupture point. Also notice that $\theta < 1$ to the right of β, satisfying $h\theta =$ constant and without any perturbation at the boundary. As indicated in that figure, the higher the value of p_{cc} the lower the fluid film thickness that exits the domain, which is consistent with the underlying physics (the CCP pushes the lubricant to the left). Also, as p_{cc} is increased, β moves away from the combustion chamber.

It is clear from the figure that a maximum value exists for p_{cc}, above which the solution does not exist. This value of p_{cc}, which is around 120 atm, corresponds to that for which the rupture point β takes the value 0.5 and also to the value of p_{cc} for which the maximum pressure in the full-film region takes place at the rupture boundary. For higher values of p_{cc} the simulation *fails* in the sense that a maximum number of iterations (=100,000) is reached without the numerical variable "*change*" becoming lower than "*tol*" in Algorithm 1. Since stationary solutions with a rupture point placed to the left of $x_1 = 0.5$ have no physical meaning, that value can be interpreted as the maximum CCP

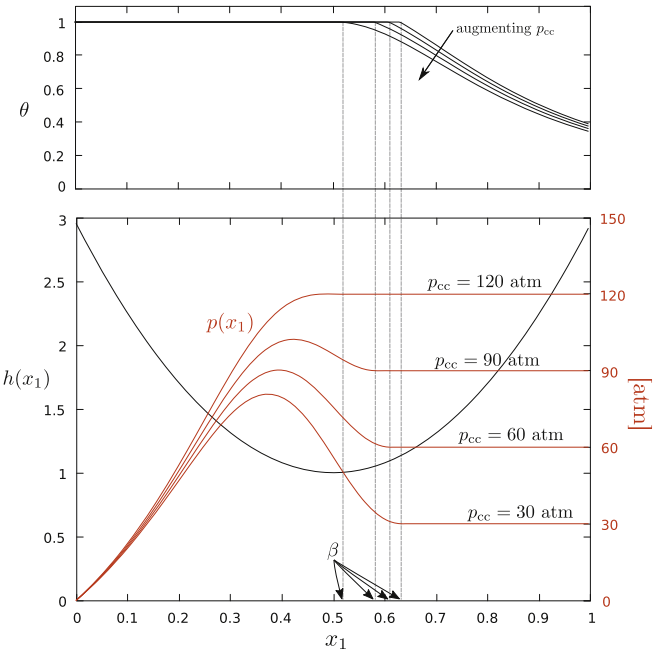

Fig. 5. Stationary solutions for $R = 64$, $u = 1$, $h_{\text{feed}} = 3$ and different values of p_{cc}.

such that the ring is able to seal the combustion chamber and prevent blow-by. As a local criterion, one observes that $\partial^2 p/\partial x^2(\beta)$ tends to zero as p_{cc} tends to its blow-by value. Based on these observations, the condition

$$\frac{\partial^2 p}{\partial x_1^2} = 0 \qquad \text{and} \qquad p > 0 \tag{27}$$

is identified as a blow-by prediction condition when the CCP acts on a film rupture boundary.

The pressure and saturation fields obtained for different values of p_{cc} when the lower surface moves to the left ($u = -1$) are shown in Fig. 6. In this case the cavitation boundary β adjacent to the combustion chamber is a reformation point. Observe that for all p_{cc} above 60 atm the pressure profiles coincide to the left of β (that depends on p_{cc}). When p_{cc} is above the maximum value of that pressure profile (about 124 atm in the case of the figure, notice that it depends in a non-trivial way on h_{feed}) the algorithm fails to converge, which makes mathematical sense since no solution can exist. The physical interpretation is again that this maximum value of p_{cc} indicates the inception of blow-by. For the case where the backpressure acts on a reformation boundary

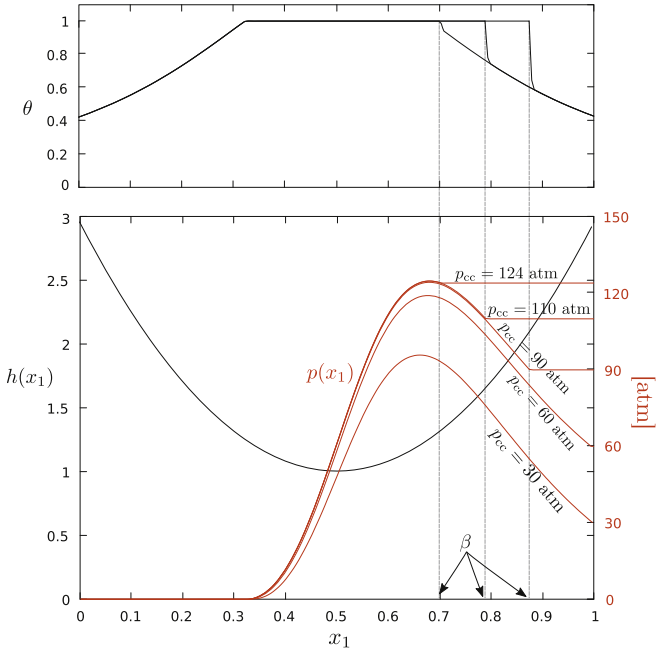

Fig. 6. Stationary solutions for $R = 64$, $u = -1$, $h_{\text{feed}} = 1.25$ and different values of p_{cc}.

it is $\partial p/\partial x_1(\beta)$ that tends to zero as p_{cc} approaches its maximum admissible value. Instead of (27), which does not hold in this case, the proposed blow-by prediction criterion when the CCP acts on a film reformation boundary is

$$\frac{\partial p}{\partial x_1} = 0 \qquad \text{and} \qquad p > 0. \tag{28}$$

4.2. Rings with textures

Consider now simulations with a texture consisting of elliptically shaped dimples on the ring (thus, corresponding to 2-dimensional simulations). The dimples are arranged at a distance equal to 0.1 along the x_2 axis, its depth is set to 1 μm and their size along the x_1 and x_2 axis is fixed to 80 and 60 μm, respectively. The ring's profile ($h_{\text{ring}}(x_1, x_2)$) is detailed in Fig. 7 along with the converged stationary fields p and θ for $u = 1$ and $p_{\text{cc}} = 50$ atm. This is a sufficiently complex case to numerically assess the well-posedness of the proposed model.

4.2.1. Convergence in space

The radial dynamics of the ring is solved as exposed in Algorithm 1,

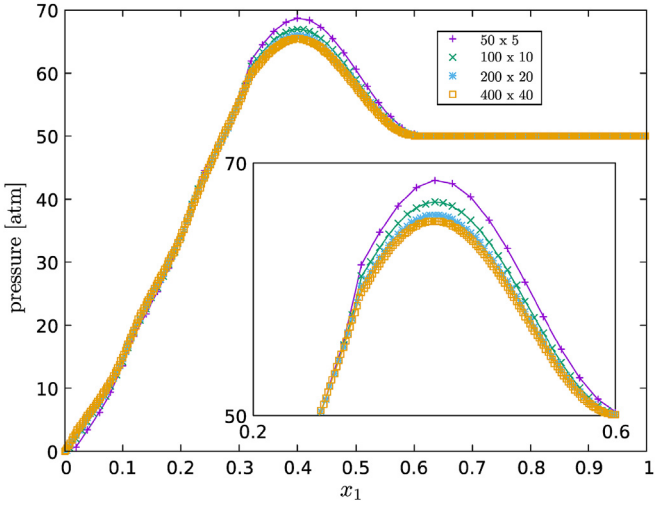

Fig. 8. Convergence of $\boldsymbol{p}$ in the stationary regime (with $u = 1$) along $x_2 = 0.05$ when varying the number of cells along x_1 and x_2.

with an initial value $Z(t = 0) = 0.8$. The cell sizes are set by taking $\Delta x_1 = \Delta x_2$ and by comparing stationary solutions obtained when fixing p_{cc} to 50 atm. These stationary solutions consist of time-converged transient simulations after a simulation time of 0.001 s, long enough for the time derivatives to be negligible. The time step is set such that the Courant-Friedrichs-Levy (CFL) number is equal to the unit.

Fig. 8 shows pressure profiles obtained along the centerline of the computational domain (i.e., $x_2 = 0.05$). Spatial convergence of the proposed algorithm is observed as the mesh is refined. Next, time convergence is addressed keeping the number of cells fixed at 200×20.

4.2.2. Convergence in time and comparison with other cavitation models

Let us now turn to transient simulations in which $p_{\text{cc}}(t)$ is taken as a Gaussian pulse that goes from non-dimensional time $t \simeq 200$ to $t \simeq 400$ and with amplitude of 50 atm, while still keeping the velocity constant in time. As shown in Fig. 9, this pulse approximates a measured CCP curve [23]. This example is quite challenging, not just because of the texture, but also because $p_{\text{cc}}(t)$ is non-monotonous, making Ω_0^r to expand and shrink dynamically along the simulation.

A convergence analysis was performed by computing the relative difference on friction in time according to

$$\Delta \bar{F}^{\Delta t} = \frac{\|F^{\Delta t}(t) - F^{\Delta t^*}(t)\|_1}{\|F^{\Delta t^*}(t)\|_1}$$

where $F^{\Delta t}$ is a discretization of (9), $\|\cdot\|_1$ is a discretization of $\int_0^{600} |\cdot|\, dt$

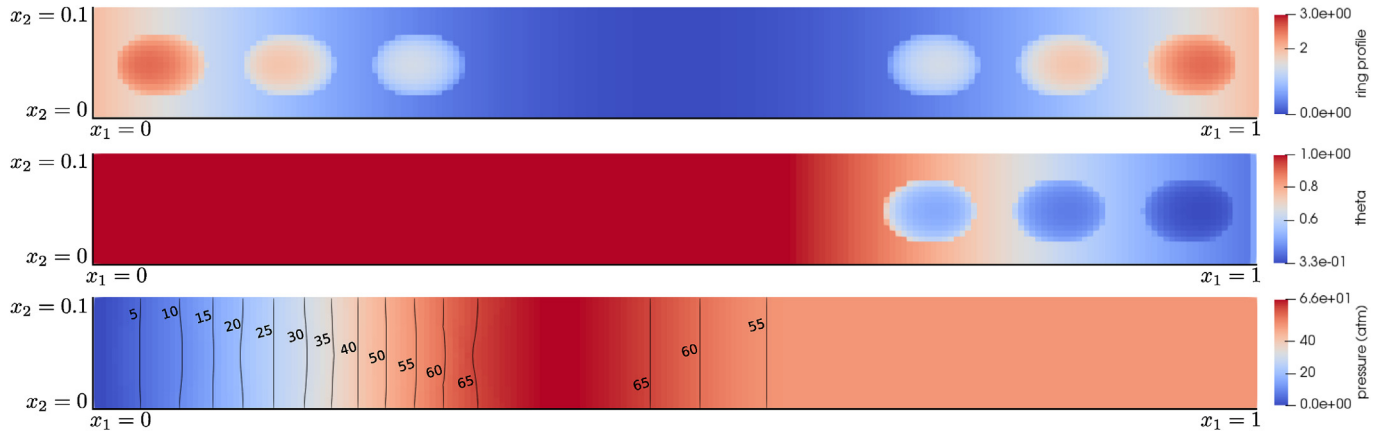

Fig. 7. Top: Profile of the textured ring, i.e., function $h^R_{\text{ring}}(x_1, x_2)$. Center and bottom: converged saturation and pressure fields.

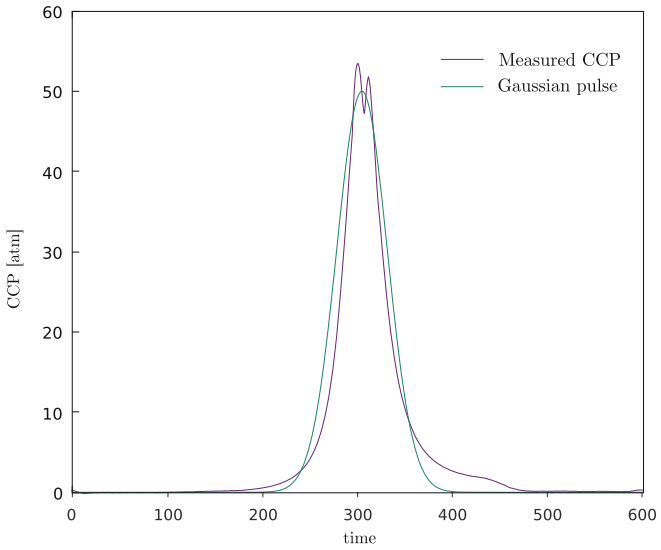

Fig. 9. Measured combustion chamber pressure as a function of time and its approximation by a Gaussian pulse.

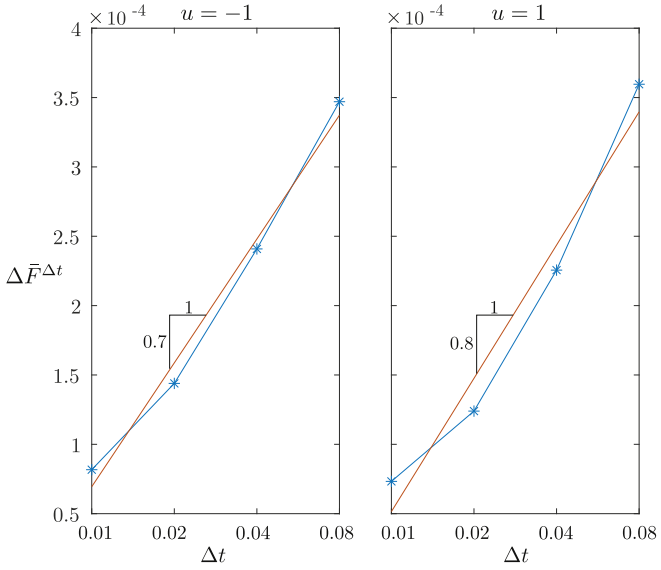

Fig. 10. Relative difference in friction for different time steps Δt, $u = -1$ and $u = 1$.

and $\Delta t^* = 0.0025$ is small enough to make time-discretization errors negligible. Fig. 10 shows $\Delta\bar{F}^{\Delta t}$ vs. Δt, considering both $u = -1$ (reformation boundary at the combustion-chamber side of the ring) and $u = 1$ (rupture boundary at the combustion-chamber side of the ring). A convergence rate of $\approx \Delta t^{0.7}$ is observed. An analogous analysis of the MFT dependence on Δt showed a convergence rate $\approx \Delta t^{0.6}$. These results suggest that the model is indeed well-posed and stably approximated, and it is thus interesting to compare it with the models previously adopted in the literature for this same problem.

For this purpose we will consider:

- the standard **Elrod-Adams model** [7,8]), which is mass-conserving but treats the hydrodynamic problem as if $p_{cc} = 0$;
- a **modified Elrod-Adams model** [12] in which the complementarity condition $p(1 - \theta) = 0$ is kept throughout the domain but the condition $p = p_{cc}$ is imposed at the right boundary even if θ there is smaller than unity; and
- the **Reynolds cavitation model**, which is not mass-conserving but nevertheless widely used [9], imposing $p = p_{cc}$ at the right boundary.

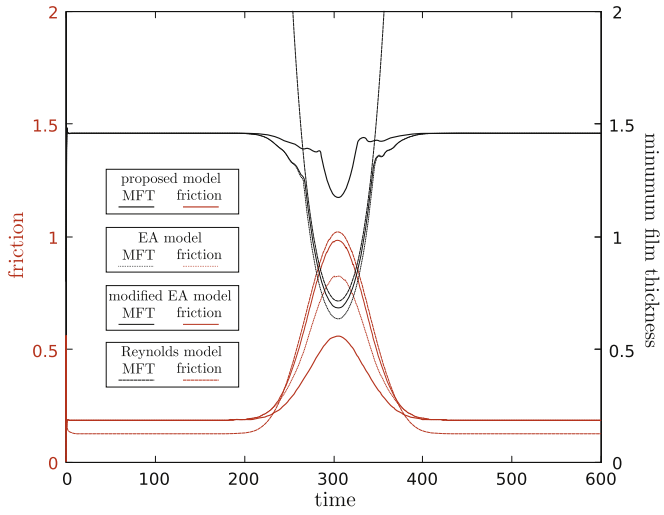

Fig. 11. Friction force and MFT obtained with the proposed model, the Elrod-Adams model (EA), the modified EA model and the Reynolds cavitation model.

The velocity and time step are set to $u = +1$ and $\Delta t = 0.01$. The comparative results for friction and MFT are shown in Fig. 11. Compared to the proposed model, all the others significantly underpredict MFT and overpredict friction significantly during the central part of the CCP pulse. At times at which $p_{cc} \simeq 0$, on the other hand, the proposed model coincides well with both variants of the Elrod-Adams model while the Reynolds model underpredicts friction and severely overpredicts MFT.

The pressure profiles along $x_2 = \pi B$ at different instants, as shown in Fig. 12, provide further insight into the previous comparison. Up to $t = 100$ all models but the Reynolds one coincide, since $p_{cc}(t)$ (and thus $T(\theta)$) is essentially zero for $0 \le t \le 100$. The Reynolds model shows the inaccuracies brought by the lack of mass conservation, since it implicitly considers the whole left half of the ring in full-film conditions, because the geometry is convergent. The profiles depicting later instants (t= 253, 300 and 347) put into evidence the improvements brought by the proposed method with respect to the Elrod-Adams variants. In the Elrod-Adams model, the whole right-hand part of the domain remains at $p = 0$ because the film is incomplete there. This is inconsistent with the actual value of p_{cc} at those instants. Turning to the modified Elrod-Adams model, it succeeds in enforcing $p = p_{cc}$ at the right boundary but only in a local way, creating a pressurized region near the (artificial) outflow boundary of the computational domain but without affecting the interior pressure. Fig. 13 shows the saturation profiles at $t = 347$, in which a region with $\theta = 1$ adjacent to the right boundary confirms the creation of a spurious full-film region there. Remarkably, a similar artifact appears when using the Reynolds model, which involves no saturation field.

4.3. Simulation of the full engine cycle considering wear

In this section both surfaces are assumed untextured, but a non-uniform analytical wear is incorporated on the ring by taking $\delta \ge 0$ and $c = 10$ in Eq. (1). Such value of c is chosen such that the wear extends $\simeq 70$ degrees along the circumferential direction x_2, which is a typical wear extension [3]. Notice that the wear can also be interpreted as taking place on the cylinder bore. Based on a convergence analysis analogous to the one presented in the previous section the cell size is set to $\Delta x_1 = 1/200$ and $\Delta x_2 = 2\pi B/40$, while the Courant number is set to 1 during most of the simulation. The film thickness at the fluid entrance is set to $h_{feed} = 1.5$. The liner's speed u (relative to the ring) and the normalized variation of $p_{cc}(t)$ are shown in Fig. 14 as functions of time

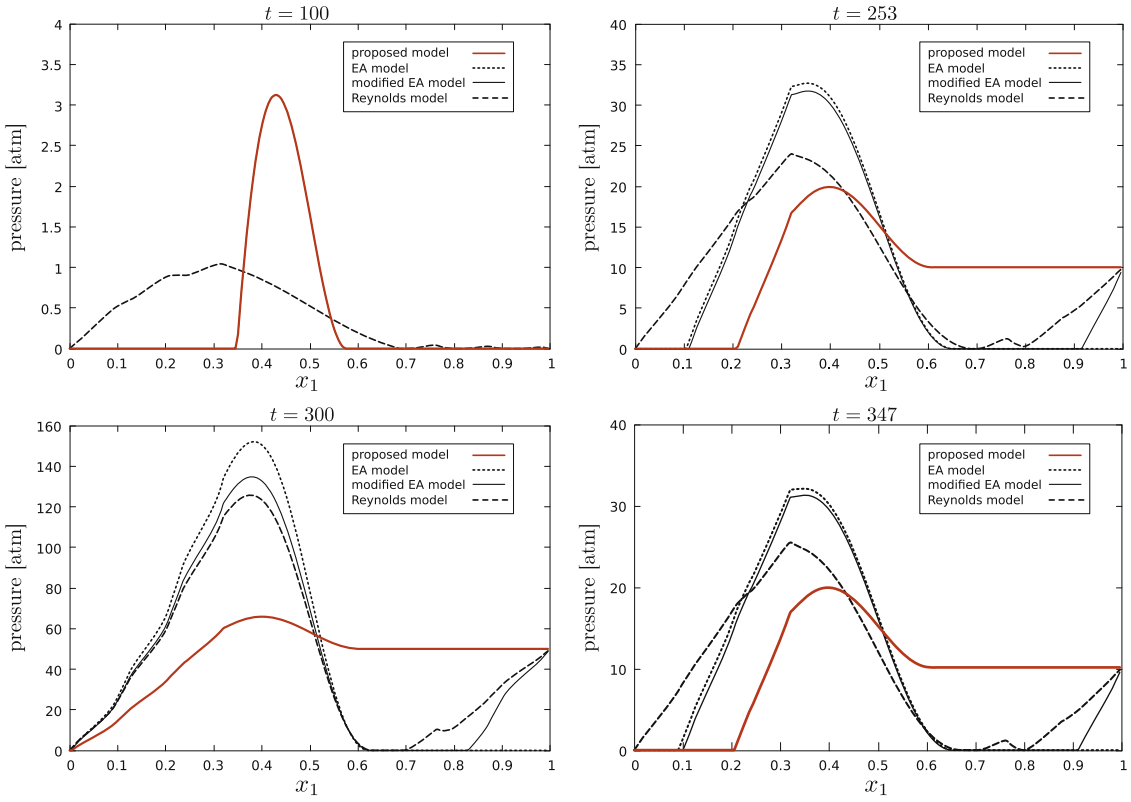

Fig. 12. Pressure profiles fixing $x_2 = \pi B$ at $t = 100$ (stationary regime, CCP $\simeq 0$), $t = 253$ (CCP $\simeq 10$ atm), $t = 300$ (CCP $\simeq 50$ atm) and $t = 347$ (CCP $\simeq 10$ atm) for different cavitation models.

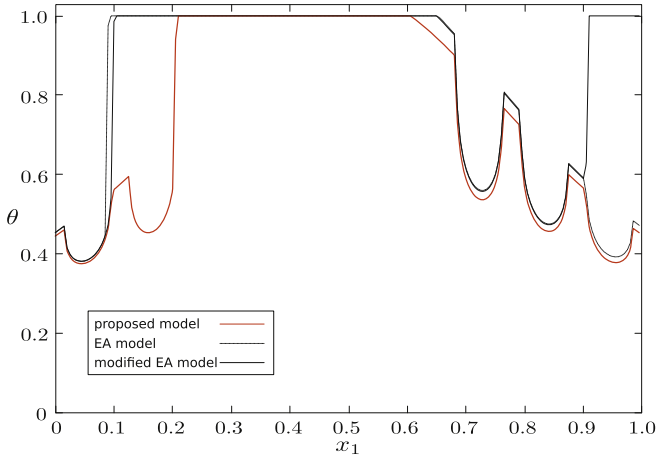

Fig. 13. Profiles of the saturation variable at time $t = 347$, corresponding to the pressure profiles of Fig. 12 (bottom right) for the different models. The Reynolds model does not appear because it does not involve a saturation variable.

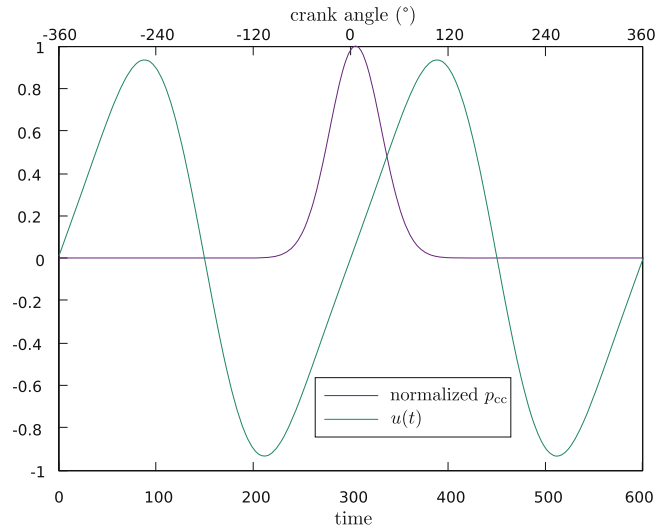

Fig. 14. Liner's speed u and CCP (normalized with its maximum value) as functions of time/crank angle to model a full four-stroke engine cycle.

and of crank angle. Some convergence difficulties that arise when $p_{cc}(t)$ is near its maximum and the speed of the ring is near 0 (at the half of the cycle) were overcome by setting the Courant number to 0.05 for $290 < t < 314$.

4.3.1. Baseline case (no wear)

The case with no wear considered on the ring (i.e., $\delta = 0$, which makes the problem independent of x_2) is used here to show some essential characteristics of the solutions obtained with the proposed model. In Fig. 15 the profiles of the pressure (p) and saturation (θ) are shown at several instants. Part (a) of the figure shows instantaneous profiles at $t = 100$, for which $p_{cc} \simeq 0$, and $t = 260$, for which $p_{cc} \simeq 12$ atm. Notice that at $t = 260$, though the liquid film is still incomplete ($\theta < 1$) near the right boundary, the CCP boundary condition is automatically enforced on the pressure field there. At $t = 298$ (part (c)) the situation has changed, because the accumulated lubricant has taken the right boundary to full-film conditions (i.e. Ω_0^r is the empty set), but the CCP boundary condition remains to hold without any numerical perturbation. At $t = 300$ (the TDC) the ring reverses its motion and, as discussed by Chong et al. [12], fluid separation occurs on the right side of the ring. As seen in Fig. 15(c) one observes that in the simulation with the proposed model a partial-film region develops soon after reversal (notice the region Ω_0^r with $\theta < 1$ near $x_1 = 1$ at $t = 300.3$). This region grows with time until at $t = 400$ the condition at $t = 100$ is

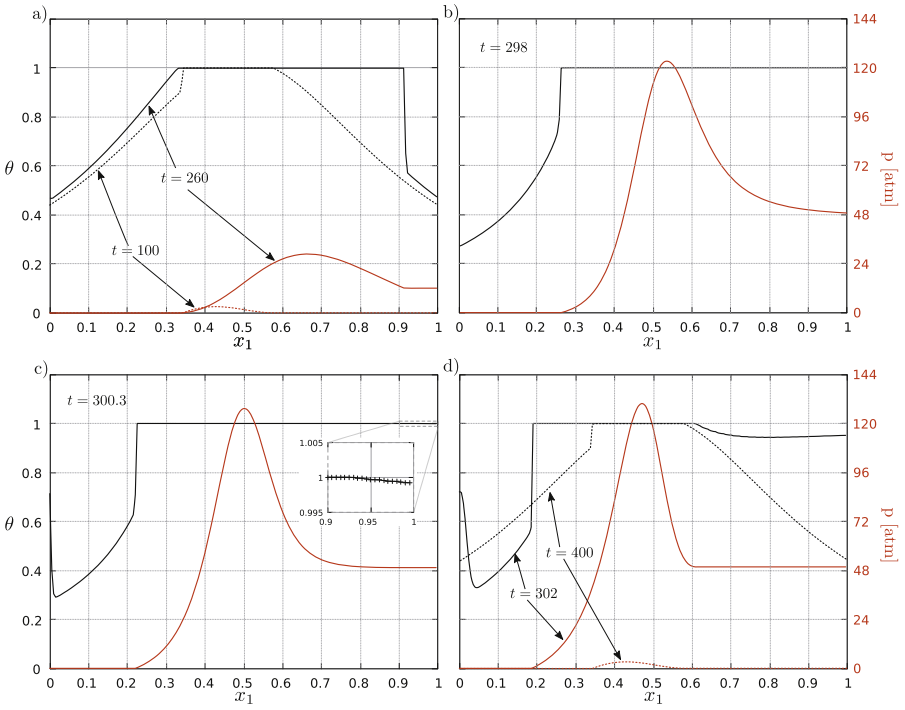

Fig. 15. Pressure (p) and saturation (θ) profiles at different times steps for the simulation without wear ($\delta = 0$).

recovered. Along this process the pressure in Ω_0^r is uniform and coincident with CCP as expected.

4.3.2. The effect of wear and blow-by inception

A series of simulations, always keeping the same CCP pulse of amplitude 50 atm, were performed considering numerous ring geometries with R ranging from 16 to 250 and δ taking the values 0.005, 0.010, 0.015, ...,0.060. It was observed that for each R there exists a value of δ, denoted by $\delta^{\max}$, such that if $\delta \geq \delta^{\max}$ the simulation fails at a certain time step before the whole cycle is completed. For any $\delta < \delta^{\max}$ the simulation is completed without difficulty, showing the robustness of the method. In fact, we claim that the failure that happens when $\delta \geq \delta^{\max}$ is not an algorithmic misbehavior but a symptom that the physical model is predicting blow-by inception. The obtained values of $\delta_{\max}$ for each ring curvature are summarized in Table 3. It is worth to notice that $\delta_{\max}$ is maximum for values of R between 42 and 50, which are typical of compression rings [24], and that for $R < 32$ even the simulations without wear crash before completion. The times of the crashes depend on both R and δ. In general, for $R < 32$ they take place at $t \simeq 300$, where p_{cc} is maximum, while for $R \geq 32$ the simulations fail earlier, when the value of p_{cc} is much smaller.

We now analyze in more detail the saturation fields obtained in the simulations to visualize the effect of wear and support our claim that simulation failure is an indication of blow-by inception. For brevity, we select just one ring curvature, $R = 62$, for which $\delta^{\max} = 0.045$ and the simulation with $\delta = \delta^{\max}$ crashes at $t = 203.2$. In Fig. 16 we show the full-film region at $t = 203.18$ for several values of δ up to $\delta^{\max}$. As the wear amplitude δ is increased, the worn sector (at the center) exhibits significant and highly localized thinning of the full-film region. As a consequence, the build-up of hydrodynamic pressure in the worn sector will be smaller than in the rest of the ring's circumference.

Table 3
Minimum value of δ for which the simulations fail for every $\delta \geq \delta^{\max}$.

	R								
	250	125	83	62	50	42	36	32	31 ··· 16
$\delta^{\max}$	0.025	0.035	0.040	0.045	0.050	0.055	0.025	0.005	0

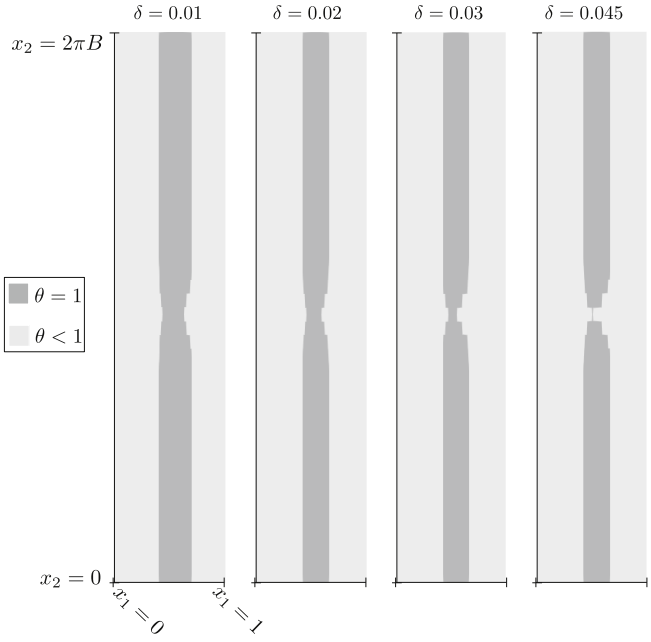

Fig. 16. Full-film regions computed at $t = 203.18$ for $R = 62$ and different values of δ. For the rightmost case ($\delta = 0.045$) the simulation crashes shortly after.

Further, it is reasonable to interpret that, at the time of the simulation crash, the model predicts a partial-film channel connecting the left and right partial-film regions (i.e., blow-by). Since these regions are at different gas pressures and the dynamics of the gas is not modeled, this provides a physical explanation of the algorithmic failure. Inspection of the pressure fields (not shown here for brevity) revealed that this explanation is also consistent with the blow-by prediction criteria (27) and (28) identified earlier in section 4.1.

4.3.3. A blow-by inception criterion

As shown in all the preceding examples, the proposed model yields physically sound solutions in many situations that are not properly

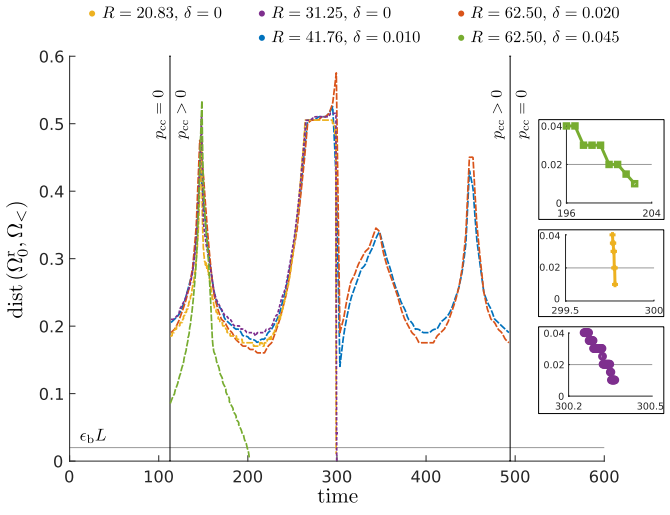

Fig. 17. Distance between the sets Ω_0^r and $\Omega_<$ as function of time for five typical simulations. The inserts on the right show a detail of the values taken by $\text{dist}(\Omega_0^r, \Omega_<)$ just before the algorithm fails to converge, for the three simulations that do not reach the end of the cycle.

represented by previous ones and, when a simulation fails for lack of convergence of the iterative algorithm at some instant, it is reasonable to interpret this fact as indicative of blow-by inception.

It is not practical, however, to have "lack of convergence" as the criterion to predict blow-by. Mathematical criteria have also been identified, namely (27) and (28), but in preliminary tests they proved to not be very robust when the involved pressure derivatives are replaced by their discrete counterparts.

Instead, we propose a numerical blow-by inception criterion that is equivalent to (27) and (28) in the exact problem but much more robust upon discretization. Let us define the subset $\Omega_<$ of the domain as the region where $p < p_{cc}$, i.e.,

$$\Omega_< = \{\mathbf{x} \in \Omega,\ p(\mathbf{x}) < p_{cc}\}. \tag{29}$$

The proposed criterion is based on the observation that, whenever the mathematical model becomes ill-posed, the distance between $\Omega_<$ and Ω_0^r tends to zero. Specifically, the criterion reads

$$\{\ \text{dist}(\Omega_0^r, \Omega_<) \le \varepsilon \quad \text{and} \quad p_{cc} > 0\} \ \Rightarrow\ \text{blow} - \text{by}, \tag{30}$$

where $\text{dist}(\cdot,\cdot)$ denotes the geometrical distance and ε is a small threshold for which we adopt the formula $\varepsilon = \max\{\varepsilon_b L, N_b \Delta x_1\}$. In what follows we take $\varepsilon_b = 0.02$ and $N_b = 4$, but the results are not very sensitive to this specific choice. In fact, a convergence analysis showed that $\text{dist}(\Omega_0^r, \Omega_<)$, as a function of time, becomes mesh-independent once the mesh is fine enough. Fig. 17 shows $\text{dist}(\Omega_0^r, \Omega_<)$ as a function of time for a few typical simulations. For the simulations that crashed it is observed that condition (30) is reached shortly before the crash (see the inserts in the figure), while for the successful simulations condition (30) is always far from being met. This qualifies (30) as a practical numerical criterion to predict blow-by inception.

5. Conclusions

A new cavitation model that accommodates non-homogeneous boundary conditions for pressure has been presented and applied to the PRL system, together with a numerical algorithm that is mass-conserving and converges in both time and space. The proposed method does not involve any adjustable parameter and yields physically sound solutions in challenging steady and unsteady problems. It is capable of simulating the full four-stroke cycle of an internal combustion engine, for which it showed significant improvements with respect to previous models from the literature. Furthermore, an easily implementable numerical criterion (observed to be mesh-independent) was proposed that allows the user of the model to predict blow-by in PRL systems.

Acknowledgments

The authors thank the financial support provided by CAPES (grant PROEX-8434433/D), FAPESP (grants 2013/07375-0 and 2018/08752-5) and CNPq (grant 305599/2017-8).

References

[1] Dowson D, Taylor C. Cavitation in bearings. Annu Rev Fluid Mech 1979;11(35–66).
[2] Han DC, Lee JS. Analysis of the piston ring lubrication with a new boundary condition. Tribol Int 1998;31(12):753–60.
[3] Cheng J, Meng X, Xie Y, Li W. On the running-in behavior of rough surface of piston rings in mixed lubrication regime. Ind Lubr Tribol 2015;67(5):468–85.
[4] a Mufti RA, Priest M, Chittenden RJ. Analysis of piston assembly friction using the indicated mean effective pressure experimental method to validate mathematical models. Proc Inst Mech Eng - Part D J Automob Eng 2008;222(8):1441–57.
[5] Checo HM, Ausas R, Jai M, Cadalen J, Choukroun F, Buscaglia GC. Moving textures: simulation of a ring sliding on a textured liner. Tribol Int 2014;72:131–42.
[6] Checo HM, Jaramillo A, Jai M, Buscaglia GC. Texture-Induced cavitation bubbles and friction reduction in the Elrod-Adams Model. Proc IMech, Part J: J. Eng. Tribol. 2015;229(4):478–92.
[7] Checo HM, Jaramillo A, Ausas R, Jai M, Buscaglia GC. Down to the roughness scale assessment of piston-ring/liner contacts. IOP Conf Ser Mater Sci Eng 2017;174(1):012035.
[8] Hu Y, Meng X, Xie Y. A new efficient flow continuity lubrication model for the piston ring-pack with consideration of oil storage of the cross-hatched texture. Tribol Int 2018;119:443–63.
[9] Kligerman Y, Shinkarenko A. Analysis of friction in surface textured components of reciprocating mechanism. Proc Inst Mech Eng J J Eng Tribol apr 2015;229(4):336–49.
[10] Usman A, Park CW. Optimizing the tribological performance of textured piston ring-liner contact for reduced frictional losses in SI engine: warm operating conditions. Tribol Int 2016;99:224–36.
[11] Chong W, Teodorescu M, Vaughan N. Cavitation induced starvation for piston-ring/liner tribological conjunction. Tribol Int 2011;44(4):483–97.
[12] Chong W, Howell-Smith S, Teodorescu M, Vaughan N. The influence of inter-ring pressures on piston-ring/liner tribological conjunction. Proc IMech, Part J: J. Eng. Tribol. 2013;227(2):154–67.
[13] Greenwood JA, Tripp JH. The contact of two nominally flat rough surfaces. Proc Inst Mech Eng 1970;185(1):625–33.
[14] Profito FJ, Vlădescu S, Reddyhoff T, Dini D. Transient experimental and modelling studies of laser-textured micro-grooved surfaces with a focus on piston-ring cylinder liner contacts. Tribol Int 2017;113:125–36.
[15] Panayi A, Schock H. Approximation of the integral of the asperity height distribution for the Greenwood–Tripp asperity contact model. Proc IMech, Part J: J. Eng. Tribol. 2008;222:165–9.
[16] Checo HM, Jaramillo A, Ausas R, Buscaglia GC. The lubrication approximation of the friction force for the simulation of measured surfaces. Tribol Int 2016;97:390–9.
[17] Jaramillo A. New models and numerical methods in hydrodynamic lubrication PhD thesis Instituto de Ciências Matemáticas e de Computação; 2019. USP.
[18] Buscaglia GC, Ciuperca I, Dalissier E, Jai M. A new cavitation model in lubrication: the case of two-zone cavitation. J Eng Math 2013;83(1):57–79.
[19] Ausas R, Jai M, Ciuperca I, Buscaglia GC. Conservative one-dimensional finite volume discretization of a new cavitation model for piston-ring lubrication. Tribol Int 2013;57:54–66.
[20] Alt HW. Numerical solution of steady-state porous flow free boundary problems. Numer Math 1980;36(1):73–98.
[21] Marini LD, Pietra P. Fixed-point algorithms for stationary flow in porous media. *Comput*. Methods Appl. Mech. Eng. May 1986;56(1):17–45.
[22] Ausas R, Jai M, Buscaglia GC. A mass-conserving algorithm for dynamical lubrication problems with cavitation. ASME J. Tribol. 2009;131(3).
[23] Wakuri Y, Hamatake T, Soejima M, Kitahara T. Piston ring friction in internal combustion engines. Tribol Int 1992;25(5):299–308.
[24] Gadeschi GB, Backhaus K, Knoll G. Numerical analysis of laser-textured piston-rings in the hydrodynamic lubrication regime. ASME J. Tribol. October 2012;134(4):1–8.